Evolution of sausage and helical modes in magnetized thin-foil cylindrical liners driven by a Z-pinch

Cite as: Phys. Plasmas **25**, 056307 (2018); https://doi.org/10.1063/1.5017849
Submitted: 30 November 2017 . Accepted: 05 March 2018 . Published Online: 26 March 2018

D. A. Yager-Elorriaga, Y. Y. Lau, P. Zhang, P. C. Campbell, A. M. Steiner, N. M. Jordan, R. D. McBride, and R. M. Gilgenbach

Evolution of sausage and helical modes in magnetized thin-foil cylindrical liners driven by a Z-pinch

D. A. Yager-Elorriaga,[1,2,a)] Y. Y. Lau,[1] P. Zhang,[1,b)] P. C. Campbell,[1] A. M. Steiner,[1,c)] N. M. Jordan,[1] R. D. McBride,[1] and R. M. Gilgenbach[1]
[1]*Department of Nuclear Engineering and Radiological Sciences, University of Michigan, Ann Arbor, Michigan 48109, USA*
[2]*Sandia National Laboratories, P.O. Box 5800, Albuquerque, New Mexico 87185, USA*

(Received 30 November 2017; accepted 5 March 2018; published online 26 March 2018)

In this paper, we present experimental results on axially magnetized ($B_z = 0.5 - 2.0$ T), thin-foil (400 nm-thick) cylindrical liner-plasmas driven with ~600 kA by the Michigan Accelerator for Inductive Z-Pinch Experiments, which is a linear transformer driver at the University of Michigan. We show that: (1) the applied axial magnetic field, irrespective of its direction (e.g., parallel or anti-parallel to the flow of current), reduces the instability amplitude for pure magnetohydrodynamic (MHD) modes [defined as modes devoid of the acceleration-driven magneto-Rayleigh-Taylor (MRT) instability]; (2) axially magnetized, imploding liners (where MHD modes couple to MRT) generate $m = 1$ or $m = 2$ helical modes that persist from the implosion to the subsequent explosion stage; (3) the merging of instability structures is a mechanism that enables the appearance of an exponential instability growth rate for a longer than expected time-period; and (4) an inverse cascade in *both* the axial and azimuthal wavenumbers, k and m, may be responsible for the final $m = 2$ helical structure observed in our experiments. These experiments are particularly relevant to the magnetized liner inertial fusion program pursued at Sandia National Laboratories, where helical instabilities have been observed. *Published by AIP Publishing*. https://doi.org/10.1063/1.5017849

I. INTRODUCTION

Recent experiments investigating axially magnetized, thin-foil cylindrical plasmas driven by the 1-MA Michigan Accelerator for Inductive Z-Pinch Experiment (MAIZE) facility at the University of Michigan[1,2] have demonstrated helical instability structures with azimuthal mode numbers $m = 0$, 1, or 2. These structures are discrete magnetohydrodynamic (MHD) modes that persist when coupled to the acceleration-driven magneto-Rayleigh-Taylor (MRT) instability. By "MHD modes," we are referring to modes devoid of the acceleration-driven MRT mechanism. Examples of MHD modes include the current-driven sausage ($m = 0$), kink ($m = 1$), and higher order helical modes ($m \geq 1$). The foil experiments conducted on MAIZE are relevant to the magnetized liner inertial fusion (MagLIF) program at Sandia National Laboratories, where an axially magnetized, laser preheated, deuterium fusion fuel is adiabatically compressed to thermonuclear conditions by an imploding cylindrical metal tube (or "liner") driven with ~19 MA by the Z Machine.[3–7] The large currents and accelerations required to implode the liner render the outer surface of the liner unstable to both the MRT instability and to the sausage ($m = 0$) and helical ($m \geq 1$) MHD modes; moreover, the MHD modes are likely coupled to the MRT instability.[8] Previous investigations on the stability of MagLIF liners observed azimuthally correlated structures when no axial magnetic field was applied[9,10] and helically oriented structures when an axial magnetic field of 7–10 T was pre-imposed.[11,12] Furthermore, the magnetized stagnation column within the fuel develops a helical structure,[6,7] suggesting that the helical instabilities in the liner may feed through to the fuel[13,14] and/or that the magnetized plasma in the fuel itself is unstable to helical modes during the strong deceleration phase, when the liner's inner surface becomes MRT unstable.[8]

Relative to the large 27-MA Z facility, investigating these instabilities at ~1 MA on university-scale pulsed power machines like MAIZE[15] offers several advantages, including reduced costs, higher shot rates, and a less destructive debris environment for developing new diagnostic techniques. However, because of the reduced driver current, imploding an initially solid liner on MAIZE requires a sub-micron wall thickness (the MagLIF liners on Z have a wall thickness of approximately 500 μm). Thus, a new platform was developed at the University of Michigan to experimentally investigate cylindrical MHD and MRT instabilities on MAIZE using aluminum liners with a wall thickness of 400 nm.[16] This platform accommodates three experimental configurations, which were designed to investigate: (1) MHD instabilities in a non-imploding geometry, where the plasma acceleration, and thus the coupling to the MRT instability, is minimized; (2) MHD-MRT coupled instabilities in an imploding geometry; and (3) the effects of the magnitude and direction of an applied axial magnetic field on a seeded $m = 1$ kink instability.

The first set of experiments demonstrated that non-imploding liners with no pre-imposed axial magnetic field developed an $m = 0$ sausage instability, whereas liners that

Note: Paper GI3 5, Bull. Am. Phys. Soc. **62**, 113 (2017).
[a)]Invited speaker.
[b)]Current address: Michigan State University, East Lansing, Michigan 48824, USA.
[c)]Current address: Lockheed Martin, Palmdale, California 93599, USA.

were magnetized with a small axial magnetic field of $B_z = 1.1$ T (small compared to the peak azimuthal field of $B_\theta = 30$ T) developed an $m = 2$ helical instability.[1]

In the second set of experiments, it was found that the $m = 0$, 1, and 2 modes persisted upon implosion, despite the coupling to the MRT instability and the rapid increase in the azimuthal magnetic field.[2] By systematically varying the axial magnetic field from one shot to the next, these investigations demonstrated that the azimuthal mode number tended to increase in a discrete fashion (with at most one or two dominant modes) from $m = 0$ to $m = 2$ as the field was increased from 0 T to 2.0 T.

The third set of experiments showed that imposing an $m = 1$ helical perturbation along the liner's inner surface yielded an $m = 1$ instability with the same helical pitch as the perturbation despite the magnitude and orientation of the applied axial magnetic field. These seeded modes thus dominated over the driven modes that arose more naturally in the first and second experimental configurations. These experiments also demonstrated that the axial magnetic field significantly reduced the instability amplitude only when the helical twist of the global magnetic field external to the liner (with combined B_z and B_θ components) was in the opposite sense to that of the plasma helix.

In this paper, we present several new experimental results for thin-foil, cylindrical liners on MAIZE. We first show that the applied axial magnetic field, irrespective of its direction (e.g., parallel or anti-parallel to the flow of current), reduces the instability amplitude for pure MHD modes (i.e., modes devoid of the MRT instability[8]). We then show that liners with applied fields of $B_z = 0.5 - 0.8$ T generate an $m = 1$ helical mode that persists not only during the implosion phase but also during the subsequent stagnation and explosion phases; additionally, these data are compared with the $m = 2$ helical mode that was previously found to persist for applied fields of $B_z = 1.1 - 2.0$ T.[2] Finally, using a 12-frame shadowgraphy system, we track individual instability bumps during the evolution of a single shot and demonstrate two important effects of mode merging: (1) we show that the merging of adjacent instability bumps may be used to explain an unexpected recurrence of *exponential* instability growth at late times and (2) we discuss how the mode merging of helical features may explain why an $m = 2$ mode is observed in the experiments when higher order modes ($m > 2$) are the first to destabilize in an analytical, ideal MHD, linear theory;[8] here, we also present new experimental evidence of helical mode merging.

II. EXPERIMENTAL CONFIGURATION

The experiments presented herein were performed on the Michigan Accelerator for Inductive Z-Pinch Experiments (MAIZE), which is a 1-MA linear transformer driver (LTD) at the University of Michigan.[15,17,18] The maximum charge voltage on MAIZE is ±100 kV. However, for the inductive liner loads used in these experiments, the charge voltage was reduced to a nominal ±70 kV to mitigate damage to the capacitors and insulators. This resulted in typical peak currents of 580 kA and quarter-wavelength risetimes of 250 ns, which were measured using B-dot probes in the transmission line. At a charge voltage of ±70 kV, MAIZE stores about 8 kJ of electrical energy in its 80 capacitors, which are distributed around the perimeter of the machine. The MAIZE LTD and load hardware are shown in Figs. 1(a) and 1(b).

The liner loads were fabricated using a rectangular (2.2 cm × 1.2 cm) aluminum foil (400-nm thick) wrapped around a cylindrical support structure, where the support structure consisted of two conducting ends (outer diameter, OD = 6.55 mm) and a dielectric center, which was either solid-cylindrical (OD = 6.35 mm) or dumbbell-shaped (OD = 1–2 mm)[16] [see Fig. 1(c)]. The solid-cylindrical support structure was used to prevent the foil from imploding, which enabled an investigation of the intrinsic MHD modes in the absence of the acceleration-driven MRT instability.[1] The dumbbell-shaped support structure was used to allow the foil to implode so that the MHD modes could couple to the MRT instability.[2]

The liner loads were axially magnetized to $B_z = 0.5 - 2.0$ T using two 80-turn Helmholtz-like coils[19] driven by a separate and independent capacitor bank (1.2 mF, 2.0 ms quarter-wavelength risetime). The two coils were separated by 2.54 cm and were situated outside of the return current can, positioned above and below the liner region to generate a spatially uniform axial magnetic field over the entire liner region (see Ref. 20 for magnetic field diffusion simulations in ANSYS Maxwell). The long risetime of the B_z coils permitted the axial magnetic field to diffuse uniformly through the load hardware and liner load prior to discharging MAIZE; in each experiment, the MAIZE discharge was initiated at the point when the axial magnetic field reached its peak value.

The primary diagnostic to investigate instability growth was a 12-frame intensified charge coupled device (ICCD)

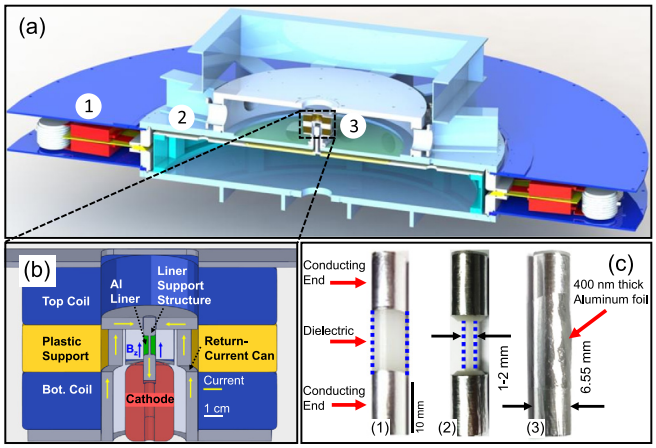

FIG. 1. (a) Cutout of the MAIZE LTD and transmission line, showing (1) the energy storage section, consisting of 40 spark-gap switches and 80 40-nF capacitors, (2) the vacuum transmission line, and (3) the load region. In (b), the load consists of a vertical, co-axial vacuum transmission line, with the cylindrical anode surrounding the central cathode stalk. The cylindrical liner load sits atop of the cathode stalk. The coaxial return-current can is slotted to enable diagnostic access to the plasma. Helmholtz-like coils surround the load to generate axial magnetic fields of $B_z = 0.2 - 2.0$ T. In (c), the liner support structures are shown for (1) non-imploding and (2) imploding configurations. For the final configuration (3), the 400-nm thick rectangular aluminum foil is wrapped around the support structure, making contact with the conducting ends.

fast framing camera, which captured liner self-emission images that were time-integrated over a 10-ns window and line filtered at 532-nm. For some of the shots, the framing camera was coupled to a 12-frame laser shadowgraphy system,[1] where a 532-nm, 2-ns pulse-length Nd:YAG laser was temporally separated into 12 beams. Using the laser backlighter resulted in a thin, dark band that outlined the self-emitting regions of the plasma, which was due to laser light being refracted out of the optical system (see Fig. 2). This band was particularly useful for tracking instability bumps early in the discharge when the liner was weakly self-emitting and later in time when instability bumps began to merge. The inter-frame time of the diagnostic was set to 10 ns when using the laser backlighter and to 25 ns when collecting self-emission only.

III. EXPERIMENTAL RESULTS AND DISCUSSION

A. Instability development in non-imploding liners

The instability development of pure MHD modes (e.g., modes devoid of the acceleration-driven MRT instability) in liners utilizing the non-imploding support structure was investigated for three axial magnetic field values, $B_z = 0\,\mathrm{T}, +1.1\,\mathrm{T}, -1.1\,\mathrm{T}$. Note that the electrical current flows in the -**z** direction. A summary of the experimental configuration and results is given in Table I. Figures 2(a) and 2(b) show shadowgraphy images of non-imploding liners for (a) $B_z = 0\,\mathrm{T}$ and (b) $B_z = +1.1\,\mathrm{T}$. In the $B_z = 0\,\mathrm{T}$ experiments, the liners developed azimuthally symmetric instability structures that are identified as the $m = 0$ sausage instability. In the axially pre-magnetized experiments, the liners developed helically oriented instability structures that are identified as the $m = 2$ helical instability, consisting of two intertwined helices that spiral in the general direction of the global, external magnetic field.[1] When the axial magnetic field was reversed, the tilt of the self-emission striations also reversed. Examining the plasma radius showed a nearly constant velocity expansion,[20] indicating that the acceleration, and thus the coupling to the MRT instability, was minimized. Therefore, these instabilities were classified as pure MHD modes.

Using either the laser shadowgraphs or the self-emission images (depending on whether or not the laser backlighter was used), the instability amplitude from each image was obtained by finding the left and right radial positions of the liner as a function of the axial position, z. The left and right instability amplitudes were then characterized by the standard deviations of the positions, σ_L and σ_R, which were multiplied by a factor of $\sqrt{2}$ to approximate the amplitude of a sine wave; the left and right amplitudes are therefore given by $A_{L,R} = \sqrt{2}\sigma_{L,R}$. The final value for the instability amplitude was taken as the mean of the left and right amplitude values, $A = (\sigma_L + \sigma_R)/\sqrt{2}$, and the uncertainty E was estimated using the difference between these values, $E = |\sigma_L - \sigma_R|/\sqrt{2}$.

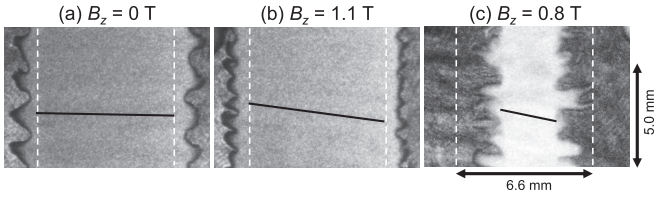

FIG. 2. Shadowgraphy images of liner-plasmas for (a) non-imploding, $B_z = 0$ (shot 1189, 326 ns), (b) non-imploding, magnetized ($B_z = 1.1\,\mathrm{T}$, shot 1190, 334 ns), and (c) imploding, magnetized ($B_z = 0.8\,\mathrm{T}$, shot 1168, 294 ns) shots. The shadowgraphy boundary is the thin, black line outlining the self-emitting plasma. The location of a sample dark self-emission striation is indicated by the black line. The approximate initial liner position is shown in white. The current is in the downward (**–z**) direction. The use of a laser line filter resulted in images made from 532-nm light; the brightness corresponds to the incident energy on the camera.

TABLE I. Summary of the experimental configuration and results for non-imploding liners. The shadowgraphy column indicates whether the laser shadowgraphy system[1] was used. The instability growth rate was measured by fitting an exponential function to the time range indicated in the timing of the fit column.

Shot No.	B_z (T)	Growth rate ($1/\mu s$)	Shadowgraphy	I_{max} (kA)	Timing of fit (ns)
1189	0	7.2 ± 0.3	Yes	560	245–345
1209	0	10.8 ± 0.5	Yes	560	120–220
1210	0	11.9 ± 0.3	No	560	175–325
1211	0	12.8 ± 0.3	No	540	170–320
1206	−1.1	9.0 ± 0.5	Yes	580	210–290
1207[a]	−1.1	…	Yes	590	…
1208	−1.1	9.9 ± 0.7	Yes	570	125–225
1212	−1.1	8.9 ± 0.2	No	590	245–345
1213	−1.1	7.7 ± 0.3	No	580	190–390
1190	+1.1	8.0 ± 0.6	Yes	570	255–325
1214	+1.1	8.5 ± 0.7	No	580	225–350
1215	+1.1	6.9 ± 0.5	No	570	215–315

[a]Amplitude data for shot 1207 in Fig. 3(a) did not have sufficient points with exponential growth to accurately measure a growth rate.

In Fig. 3, the instability amplitude as a function of time is presented. The shadowgraphy data [Fig. 3(a)] have larger amplitudes when compared to the self-emission only data [Fig. 3(b)]. This is simply because the shadowgraphy boundary is at a larger radius than the self-emission boundary. Despite this approximately constant offset difference, the two methods resulted in very similar growth rates (see Table I).

To measure the instability growth rate, we fit only the exponentially growing regions (identified on a semi-log plot) using the equation $A = A_0 \exp(\gamma t)$, where A is the instability amplitude at time t, A_0 is the fitted amplitude at $t = 0$ (corresponding to the start time of the current), and γ is the instability growth rate. The amplitude A_0 is not the true instability seed amplitude at $t = 0$ but rather a parameter that characterizes the amplitude of the structures that seeded the observed instability. The fitted curves excluded early-time data points (where the amplitude change from image-to-image was negligible) and late-time data points (where saturated/non-exponential instability growth was observed). From these fits, summarized in Table I, we see that the axial magnetic field slightly reduced the instability growth rate when compared to the $B_z = 0\,\mathrm{T}$ case (with the exception of shot 1189, discussed below); nevertheless, the cumulative effect of applying the axial magnetic field is that the overall instability amplitude is significantly reduced when compared to the $B_z = 0\,\mathrm{T}$ case (see Fig. 3).

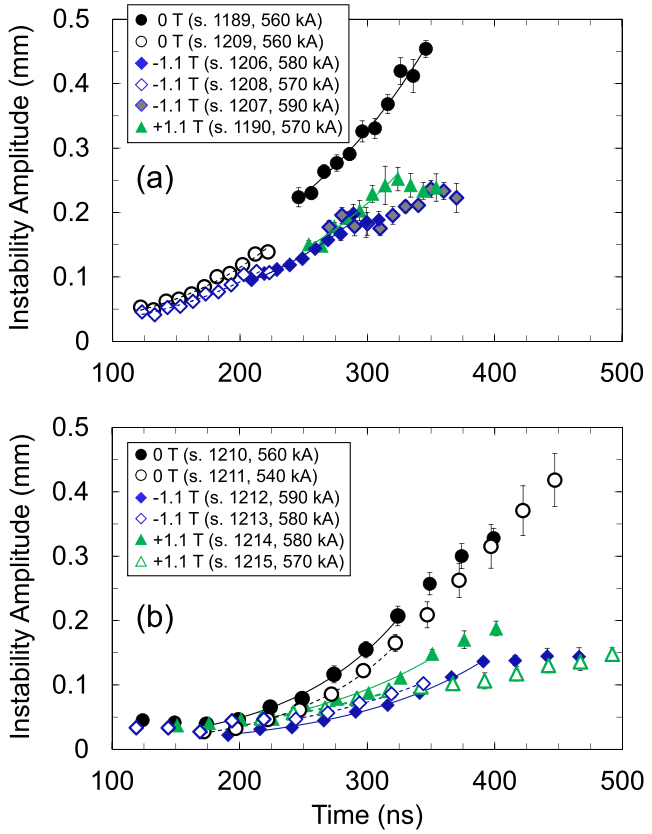

FIG. 3. Experimental instability amplitudes measured using (a) the laser backlighter and (b) self-emission only. The plots show exponential curves, fit only to the exponentially increasing time periods (identified on a semi-log plot), which give measurements of the instability growth rates, summarized in Table I.

Shots with data after 300 ns showed saturation in the instability development (see Fig. 3). For the shadowgraphy diagnostic, amplitude data for both axially magnetized cases actually decreased in time, as shown in Fig. 3(a), while for the self-emission only diagnostic, the saturation was characterized by an algebraically increasing instability growth (i.e., the amplitude growth is linearly proportional to time), as shown in Fig. 3(b). This saturation occurs later in time for the axially pre-magnetized experiments (between 350 and 400 ns) than for the $B_z = 0$ T experiments (~325 ns), which may be attributed to the smaller ratio of instability amplitude to axial wavelength for the magnetized liners (see Sec. III C). Note that this saturation likely explains the slightly smaller growth rate for the $B_z = 0$, $m = 0$, shot 1189 data, which were captured later in time ($t = 245 - 345$ ns) when the saturation and instability merging process had already begun.

Changing the direction of the axial magnetic field from $B_z = -1.1$ T (parallel to current) to $B_z = +1.1$ T (anti-parallel to current) did not have a significant effect on the instability growth rate (see Table I); however, differences were observed in the instability amplitude. Data with the axial magnetic field directed anti-parallel to the flow of current tended to have a slightly larger instability amplitude when compared to the parallel orientation (see data for shots 1190 and 1214 in Fig. 3) with the notable exception of shot 1215 ($B_z = +1.1$ T), which had a comparable instability amplitude to shot 1212 ($B_z = -1.1$ T). Interestingly, the peak current, and thus the azimuthal magnetic field which ultimately drives the instabilities, was larger for shot 1212 (590 kA) than for shot 1215 (570 kA). Taking this into account, along with the observation that shots 1190 and 1214 ($B_z = +1.1$ T) had noticeably larger instability amplitudes, suggests that the instability development may indeed be slightly larger when the axial magnetic field is directed anti-parallel to the flow of current. In ideal MHD, there is no difference in linear growth rates between an axial field that is parallel or anti-parallel to the direction of current flow; however, in more sophisticated MHD models (e.g., models that include the Hall term in the generalized Ohm's law[21]), the growth rates can depend on whether the axial field is parallel or anti-parallel to the direction of current flow. The data presented here motivate future investigations to determine whether this effect is due to the stochastic nature of instability development or if it originates from a physical mechanism dependent on the orientation of the applied axial magnetic field.

To interpret the experimental data, we used the Weis-Zhang-Lau (WZL) theory[8] to calculate the instantaneous theoretical sausage and helical growth rates. These are presented in Fig. 4, which shows contour plots of the instantaneous growth rate as a function of time for azimuthal mode numbers ranging from $m = -12$ to $m = +12$ and for axial magnetic fields of (a) $B_z = 0$ T and (b) $B_z = 1.1$ T. These calculations require values for the plasma radius, instability wavelength, plasma density, liner thickness, and instantaneous magnetic field, which were either measured from the experiment or estimated using reasonable parameters based on simulations.[20] Despite the observation that the instability wavelength changes over time, its value was fixed at $\lambda = 0.3$ mm, which is the wavelength that first appears in the experiments. This value could incorporate the time-changing effects observed in Sec. III C; however, doing this would primarily change the numerical values for the growth rate and unnecessarily complicate the interpretation of the growth rate plots presented in Fig. 4. Other model parameters include: (a) the liner radius (fixed at a radius of 3.5 mm for ease of calculation); (b) the magnetic field (determined from the plasma radius in the experimental images and from the driving current pulse, which was approximated by a half-wave sinusoidal function with a peak current of 580 kA and a base-to-peak risetime of 250 ns); (c) the liner thickness (estimated to be about 0.2 mm); and (d) the plasma density (set to 4.5 kg/m^3, which was obtained from interferometry measurements of electron density at the edge of the plasma[20]). Modifying these parameters primarily affects the absolute numerical value of the growth rates for a given point in time; it does not significantly affect the relative trends observed with our analysis.[20]

As shown in Fig. 4(a), when there is no axial magnetic field, the most unstable mode is the $m = 0$ sausage mode for all times, and the negative m modes have the same growth rate as the positive m modes. These results are intuitively expected because the $m = 0$ mode requires no bending of the azimuthal magnetic field and because, in the absence of an axial magnetic field, a plasma helix spiraling up or down experiences the same magnetic tension. Thus, we would

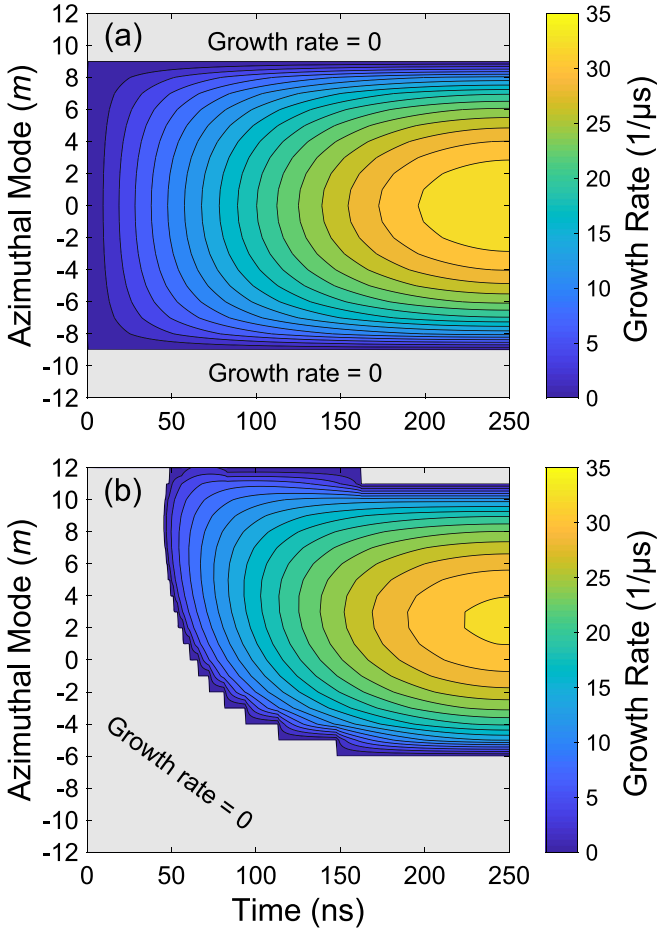

FIG. 4. (a) and (b) Weis-Zhang-Lau analytical instability growth rate calculations for non-imploding liners (no MRT coupling) with small wavelength perturbations ($\lambda = 0.3$ mm) for (a) $B_z = 0$ T and (b) $B_z = 1.1$ T. These calculations use a typical current pulse (580 kA peak current, 250 ns base-to-peak rise-time), a liner thickness of $\Delta = 200\,\mu$m, and a plasma density of $n = 10^{20}/\text{cm}^3$. The plot in (b) shows a region in time of 45 ns where all modes are stable. As time progresses, higher order modes de-stabilize, beginning with the $m = 9$ mode. The $m = 4$ mode has the largest growth rate when the instability bumps are first resolvable ($t = 120$ ns), indicating that this may be the first mode that develops in the experiments (see Sec. III D and Fig. 9).

expect the $m = 0$ mode to dominate, which was indeed the mode observed in the experiment [Fig. 2(a)].

In Fig. 4(b), we present the dramatic effect of adding a relatively small axial magnetic field of 1.1 T (the peak azimuthal field for these calculations was 33 T). First, the regions of high growth rate shift to positive m modes, an intuitive consequence as these modes have a smaller magnetic tension when compared to the negative m modes. We also see that there is a region of complete stability, where all azimuthal modes are stable for $t < 46$ ns. At $t = 46$ ns, the $m = 9$ mode is the first to destabilize. Interestingly, this mode destabilizes before even higher order modes with $m > 9$. As determined in the experiment, the first detectable instability bumps are observed around ~120 ns. Using Fig. 4(b), we see that at $t = 120$ ns, the $m = 4$ mode has the largest growth rate. Assuming that the MHD modes may develop at $t = 120$ ns, we would expect the $m = 4$ mode to dominate. Helical mode merging, discussed in Sec. III D, may also explain this dominance of the $m = 4$ mode at $t = 120$ ns, seeded from the $m = 8$ mode at $t = 46$ ns, as well as the experimental observation of an $m = 2$ mode at the final stage, despite higher order modes becoming the first to de-stabilize in the theory.

B. Discrete $m = 1$ and $m = 2$ helical modes in imploding liners

Using the dumbbell-shaped support structure enabled the liners to undergo complex dynamics, including an implosion ($\mathbf{v} < 0$), stagnation ($\mathbf{v} \approx 0$, $\mathbf{a} > 0$), and subsequent explosion stages ($\mathbf{v} > 0$), where $\mathbf{a}$ and $\mathbf{v}$ are the radial acceleration and velocity vectors.[2] A sample shadowgraphy image of a magnetized liner ($B_z = 0.8$ T) during the implosion is shown in Fig. 2(c), and a summary of the experimental parameters is given in Table II. Throughout the implosion stage and before the stagnation stage, the outer plasma interface was susceptible to the acceleration-driven MRT instability, which was found to couple to the MHD modes observed in the non-imploding geometry in Sec. III A. The important question of whether the initial MHD helical instability modes persist during the implosion, when other MRT modes may simultaneously develop, is investigated in the remainder of this section.

The axially pre-magnetized liners revealed tilted self-emission striations that increased (decreased) in pitch angle during the implosion (subsequent explosion) stage, when the plasma radius was decreasing (increasing). These striations were dark and bright relative to the overall liner self-emission and were found to connect instability bumps and necks across the plasma, respectively. Figure 5 shows a representative set of contrast-enhanced bright and dark striations during the implosion stage ($B_z = 1.1$ T, shot 1172) and a single bright striation during the explosion stage ($B_z = 2.0$ T, shot 1158); both figures track the same striations at two different points in time, as indicated in the figure. The striation pitch angle was measured by taking the slope of a linear regression fit to the self-emission local minima and maxima (see the solid black and white lines in Fig. 5), which were identified using a tracking algorithm.[1]

To understand the dynamics of the striation angles, we examine the perturbation for cylindrical MHD modes, $\exp(im\theta - ikz)$, where m and $k = 2\pi/\lambda$ are the azimuthal number and axial wavenumber (with axial wavelength λ), respectively. These modes result in instability structures consisting of m intertwined helices,[1] whose helical pitch angle is found by tracing a perturbation along a constant phase C so that $im\theta - ikz = C$. Differentiating yields the relationship

TABLE II. Summary of experimental parameters for imploding liners. The azimuthal mode number is identified for at least one image in the discharge using the procedure outlined in Ref. 1.

Shot	B_z (T)	Azimuthal mode (m)	I_{max} (kA)	Image timing (ns)
1166	0.5	1	530	298–348
1168	0.8	1	550	274–314
1172	1.1	2	580	240–290
1169	1.6	2	570	272–292
1158[a]	2	2	…	308–389

[a]Current trace not available.

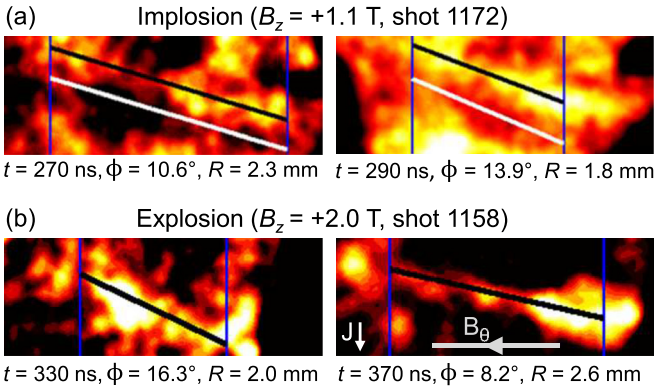

FIG. 5. Self-emission striations for (a) implosion and (b) explosion data. The same bright and dark striations are tracked from image to image, showing an increase in the striation angle during the implosion stage and a decrease in the striation angle during the explosion stage. The direction of the current density $\boldsymbol{J}$ and azimuthal magnetic field B_θ are indicated in (b). The axial B field is in the $+z$ direction.

$\mathrm{d}\theta/\mathrm{d}z = k/m$ so that the pitch angle along this constant phase may be determined as follows:[8]

$$\phi = \mathrm{atan}(\mathrm{d}z/R\mathrm{d}\theta) = \mathrm{atan}(m/kR) \sim m/kR. \quad (1)$$

Note that the last approximation is applicable for small angles, such as those measured in these experiments. Thus, for a helical mode with m and k constant, the helical pitch angle increases (decreases) as the plasma radius decreases (increases) during the implosion (explosion) stage of the discharge, consistent with our experimental data. Weis *et al.*[8] showed that this interpretation was also consistent with the temporal evolution of the helical pitch observed in the Sandia experiments.[11,12]

The relationship in Eq. (1) may be used to identify discrete helical modes that vary in radius as the plasma implodes and explodes by plotting the measured pitch angles observed in self-emission against $1/kR$, where k and R are the mean axial wavenumber and plasma radius for a given image. For each image, the pitch angle was taken as the mean of all pitch angles from bright and dark striations, with uncertainty determined using the standard error in the dataset. The angles are modified by a factor of $2/\pi$ to account for the 3-D structure of the helix.[22] The mean wavenumber was determined using the mean wavelength, calculated by averaging the distances λ_i between the centers of all adjacent bumps (both vertically and radially, identified manually), and the mean radius was determined by averaging the radii R_i for all distinguishable instability bumps, where R_i is the distance from the center of an instability bump to the **z**-axis (determined using the pre-shot liner shadowgraph). Note that the uncertainties (estimated using the standard deviation) in the mean values k and R are much larger than the uncertainties in the individual measurements λ_i and R_i. In other words, the errors made in choosing an individual λ_i and R_i have little impact on the mean values.

For each image, the self-emission pitch angles were measured independently of the plasma radii and wavelengths and were used to generate a scatter plot of the measured pitch angles against $1/kR$ (see Fig. 6). The data are plotted for both the implosion and subsequent explosion stages, and they are marked in red or black when helical structures with one (red, $m = 1$) or two (black, $m = 2$) intertwined helices are present for at least one image during the discharge (the helical mode identification procedure follows that outlined in Ref. 1). In Fig. 6, the required one-to-one fits between the pitch angles and $1/kR$ for an $m = 1$ and $m = 2$ mode are plotted using red and black lines, respectively (recall that the helical pitch angle is $\phi = m/kR$; thus, the slope of these lines is determined by the mode number). Comparing these lines with the experimental data points in red and black shows an overall good agreement, indicating the *persistence of these helical modes throughout a period of time that includes implosion, stagnation, and explosion*. It is remarkable that these structures maintain their coherence/identity throughout this period since very disparate dynamical processes are involved. This figure also demonstrates the discrete increase from $m = 1$ to $m = 2$ due to the increase in the applied axial magnetic field from $B_z = 0.8$ T to $B_z = 1.1$ T. Increasing the field beyond $B_z = 2.0$ T is likely to yield even higher order modes with $m \geq 3$; this work is left for future experiments.

C. Mode merging and the recurrence of exponential growth

A particularly interesting feature of Fig. 3 is the appearance (or recurrence) of an exponentially growing instability amplitude for over 300 ns, despite the linear theory (which describes exponential growth in time) being applicable for only "small amplitude perturbations." The data in Fig. 3

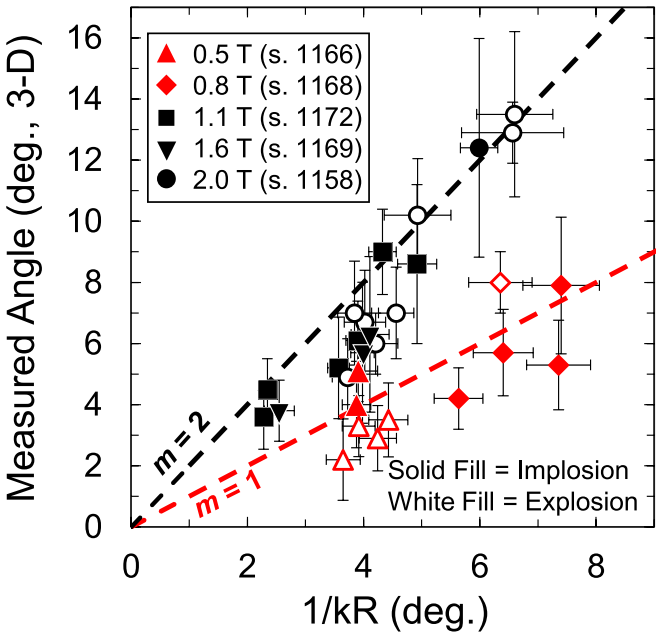

FIG. 6. Plot of measured striation angle versus $1/kR$, the predicted helical pitch angle ($\phi = m/kR$) divided by the azimuthal mode number, m. The data are plotted in red or black when one or two intertwined helices are identified[1] in the shadowgraphy/self-emission images, respectively. The data show an overall agreement with the required lines for the $m = 1$ (red, dashed) and $m = 2$ (black, dashed) modes during both the implosion and explosion stages of the discharge, indicating the persistence of discrete helical modes.

indicate that saturation occurred during the late-time growth of the instability features (saturation causes the growth rate to depart from an exponential time dependence). Additionally, the corresponding image data reveal the merging of instability bumps, which results in a time-changing wavelength. Investigating these observations further, we tracked the ratio of the instability amplitude, A, to wavelength, λ (measured using the plasma boundary, see Ref. 20). This ratio, $A/\lambda = kA/2\pi$, characterizes the applicability of the linear perturbation theory. When kA is small, the instability growth may be modeled by linear perturbation theory (recall that the product kA can be used as the dimensionless expansion parameter in a nonlinear theory). The linear theory, which yields simple exponential growth, fails[23] if $kA > 1$, i.e., if $A/\lambda > 0.16$. The values of instability wavelength are plotted as a function of time for shot 1189 ($B_z = 0$ T) in Fig. 7(a) and show a discrete increase between 266 ns and 286 ns, where the wavelength approximately doubled from $\lambda = 0.9$ mm to $\lambda = 1.7$ mm after synchronous merger events. Figure 7(b) shows enlarged images for the four frames indicated in Fig. 7(a). The images show the detailed process of two, smaller wavelength instability structures merging into a single, larger instability structure.

Using these data, the mechanism for the recurrence of exponential growth may be qualitatively understood as follows. First, assume that $kA = 1$ (or $A/\lambda = 0.16$) marks the transition between the linear and nonlinear development of the instability. The linear perturbation theory is characterized by exponential growth in perturbations for small A/λ. When the amplitude is no longer small, in particular if $A/\lambda > 0.16$, the nonlinear theory must be applied. In Fig. 7(a), we plot the ratio A/λ as a function of time (for the left side of the liner only), using both the shadowgraphy and self-emission data. Before the merging process occurs ($t < 266$ ns), this ratio of A/λ increases to 35% and 23% for the shadowgraphy and self-emission data, respectively. Both these values are well beyond the applicability of the linear perturbation theory, and thus, it appears as though the growth of these modes has temporarily saturated. This saturation does not last long, however, due to the merging of instability structures. During this merging process, the amplitude remains nearly unchanged, but because the wavelength rapidly *increases*, the ratio A/λ rapidly *decreases* to 19% and 10% for the shadowgraphy and self-emission data, respectively, so that the linear theory might become applicable again (e.g., the importance of the non-linear terms in the expansion in kA is reduced) and exponential growth ensues. After merging ($t > 286$ ns), the wavelength remains approximately constant for the remainder of the shot.

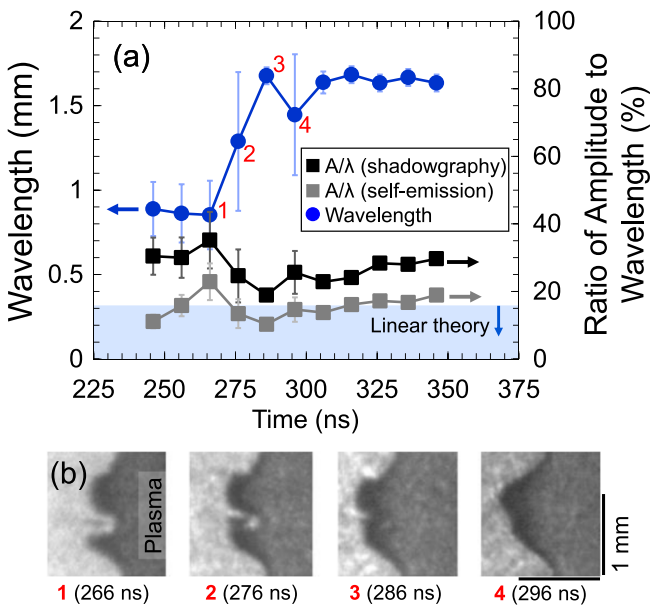

FIG. 7. (a) Instability wavelength and ratio of amplitude to wavelength for the $B_z = 0$, $m = 0$ sausage mode in shot 1189. The data are plotted for the left side of the liner, which showed synchronous merger events. The ratio of amplitude to wavelength is plotted using both the shadowgraphy and self-emission boundaries. (b) Detailed process of instability bump merging. Data points marked in red in (a) correspond to the frames in (b). The data show that during the merging process, a rapid increase in wavelength is accompanied by a rapid decrease in the ratio of amplitude to wavelength, which allows the subsequent instability growth to remain closer to the linear theory (albeit with a smaller growth rate due to the increase in wavelength).

Here, an important distinction must be made between the *merging* of instability modes and the *competition* of modes from an initial spectrum of perturbations. In other words, one must determine whether adjacent, small wavelength instability bumps merge to form a single larger bump or smaller wavelength structures saturate and are overtaken by longer wavelength modes with a larger saturation amplitude. Using the argument given in the preceding paragraph, longer wavelength structures should have a larger saturation amplitude, $A_{sat} = 0.16\,\lambda$; thus, one would expect that, in both cases, larger wavelength structures should emerge. To address this distinction, we must consider the dynamics of instability bumps in addition to the evolution of the power spectrum of wavelengths. We focus on the $B_z = 0$ T data, particularly shots 1189, 1210, and 1211, which developed instability structures with larger amplitudes (Fig. 3) and wavelengths when compared to the axially magnetized data, facilitating the identification of instability bump peaks. Shots 1210 and 1211 were particularly useful for this analysis, as they captured the late time behavior of the $m = 0$ mode (the latest image times were 400 ns and 445 ns, respectively) and exhibited multiple merger events throughout the 275 ns imaging window.

Figure 8 presents a representative dataset from shot 1211, showing (a) the plasma-vacuum interface, (b) the evolution of the instability wavelength, and (c) the wavelength power spectrum at various times during the discharge. In Fig. 8(a), the peaks of the instability bumps were found using the *findpeaks* algorithm in MATLAB and are marked as triangles in the plot. These peaks are tracked from frame to frame using the dashed lines, which show multiple two-to-one merger events. In Fig. 8(b), the wavelength was measured using a "mean-crossing" method, which determines a single characteristic wavelength by counting the number of crossings between the plasma interface and the mean radius (see Ref. 20). This plot captures the discrete increase in wavelength as a function of time from $\lambda = 0.6$ mm to 1.1 mm to 1.9 mm due to the merging events identified in (a). While the data in Figs. 8(a) and 8(b) argue for mode merging (e.g., the peaks of instability bumps move closer together and join, and the wavelength increases in a discrete fashion), we must still determine whether these longer wavelength modes

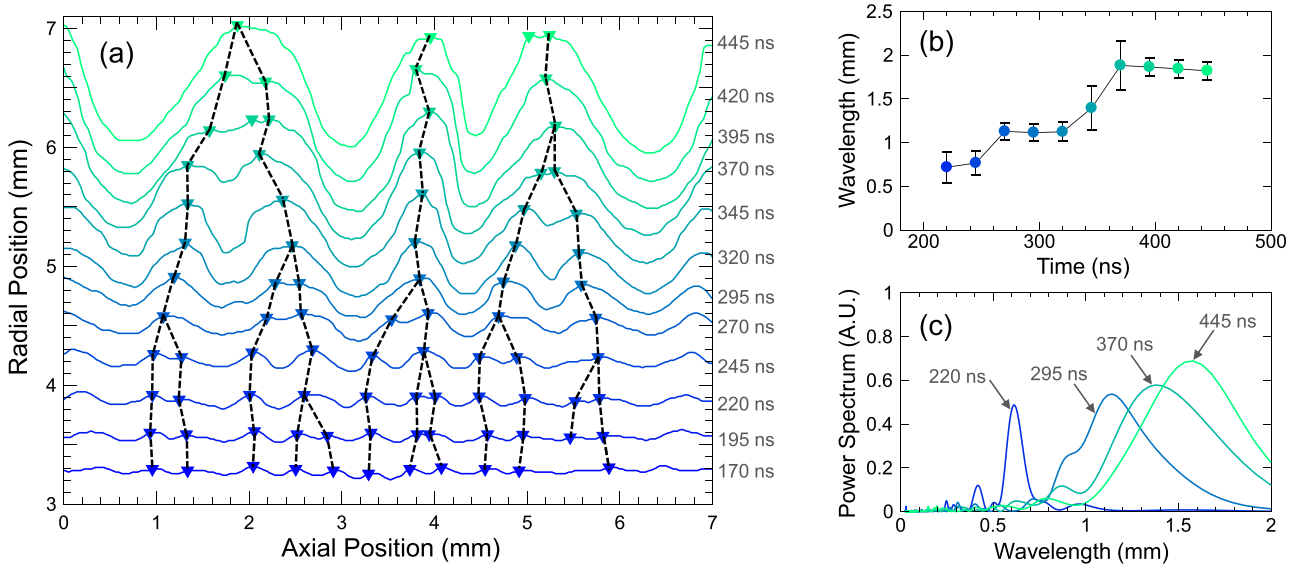

FIG. 8. (a) Radial positions for shot 1211 ($B_z = 0$ T), offset by 0.2 mm per frame (the plotted radii are given by $R_{plot}(t_n) = (n-1)\cdot 0.2\,\text{mm} + R_{measured}(t_n)$, where $R_{measured}(t_n)$ is the measured radius of the nth frame at time t_n, with $t_1 = 170$ ns, $t_2 = 195$ ns, etc.). The dashed lines track the position of local maxima (triangles) from frame to frame and show the merging of instability bumps. (b) The instability wavelength determined using a "mean-crossing" method (see Ref. 20) for the data in (a), showing a nearly discrete increase from $\lambda = 0.6$ mm to 1.1 mm to 1.9 mm. (c) Wavelength power spectrum of radial positions in (a), determined using the Fast Fourier Transform. A Hanning window and zero-padding were applied.

(e.g., $\lambda = 1.1$ mm and 1.9 mm) arise from *competition* with other modes. In Fig. 8(c), we plot the power spectrum of wavelengths of the data in (a) (determined using the Fast Fourier Transform of the plasma radius with an applied Hanning window and zero-padding) at times $t = 220$ ns, 295 ns, 370 ns, and 445 ns, and we find that the data are inconsistent with mode competition. First, we see that the dominant mode at 220 ns ($\lambda = 0.6$ mm) is nearly absent at later times and has almost completely disappeared at $t = 295$ ns. This is inconsistent with mode competition, where one would expect the 0.6 mm mode to continue developing beyond saturation, although with a smaller growth rate than the longer wavelength modes that have not yet saturated. Furthermore, the $t = 295$ ns spectrum shows a dominant peak at 1.2 mm—for mode competition, this mode must have existed at some level (along with competing modes) at an earlier time; however, this was not the case. While the $t = 220$ ns spectrum indeed shows multiple peaks (with a dominant peak at 0.6 mm), the power spectrum amplitude is nearly zero at 1.2 mm, indicating that this mode did not exist at this earlier time. Thus, the 1.2 mm wavelength mode must have developed due to some mechanism other than mode competition, the other mechanism in this case being the merging of adjacent 0.6 mm wavelength bumps to form a 1.2 mm structure. As we found these observations to be true for all shots considered ($B_z = 0$ T), we conclude that mode merging is the dominant mechanism responsible for the increase in instability wavelength. We caution that this conclusion is supported for the observed data (typically with $t > 200$ ns) and that it is possible that mode competition could have occurred earlier, before the instability bumps are resolvable ($t < 100$ ns).

D. Helical mode merging

The merging process of the instability bumps for the $m = 0$ MHD sausage mode described in Sec. III C for the $B_z = 0$ T, non-imploding liner is similar to the merging of MRT modes,[24] as both processes result in an inverse cascade of the axial wavenumber k. In the case of a well-developed $m = 0$ structure (e.g., the structures have correlated azimuthally), the azimuthal mode number ($m = 0$) remains unchanged throughout the merging process. This is not the case for helical modes, where the merging results in an inverse cascade in *both* k and m. This is a necessary geometric effect: consider a helical perturbation with azimuthal and axial mode numbers m_0 and k_0 which undergoes a merging process where adjacent instability bumps merge in a two-to-one fashion. Since the azimuthal mode number is interpreted as the number of intertwined helices,[1] this merging corresponds to the merging of individual helical perturbations. Thus, the post-merging structure has mode numbers of $m = m_0/2$ and $k = k_0/2$. The pitch angle of the helices, $\phi = m/kR$, is not affected by the merging due to the *simultaneous reduction* in m and k. Note that the final possible result of this cascade of helical modes is the $m = 1$ mode and not the $m = 0$ mode.

Figure 9 shows the axially magnetized, non-imploding liner of shot 1190 undergoing the merging of adjacent

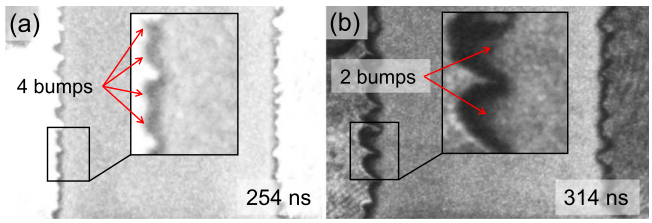

FIG. 9. Shadowgraphy images for a non-imploding, magnetized liner ($B_z = 1.1$ T, shot 1190) showing evidence of helical mode merging. The enlarged regions show four bumps at 254 ns (a) which merge to form two bumps at 314 ns (b). This may be interpreted as the $m = 4$ mode merging to generate the $m = 2$ mode (the latter is identified using a tracking algorithm of self-emission structures[1]). However, the $m = 4$ mode cannot be identified in self-emission due to a low signal-to-noise ratio.

instability bumps. An enlarged region in the images shows that four instability bumps merge to form two instability bumps. Since these later time (314 ns), longer-wavelength structures correspond to an $m=2$ helical mode, it is possible that these early-time (254 ns) structures correspond to an $m=4$ mode. A caveat to this interpretation is that the $m=4$ mode cannot be clearly identified in the image taken at 254 ns. Due to the lack of self-emission striations, the small wavelength instability features cannot be connected across the plasma and the method to identify the azimuthal mode number in Ref. 1 cannot be applied. An alternative interpretation is that by 254 ns, the *general* form of the $m=4$ mode has developed (or perhaps even the $m=8$ mode with a smaller axial wavelength)—the instability bumps have developed in a tilted pattern but have not linked completely about the circumference of the liner. By 314 ns, the $m=2$ mode cannibalizes these incomplete helix-like structures to generate a coherent structure consisting of two intertwined helices.

These interpretations are consistent with the WZL analytical calculations in Fig. 4. Following a period of time where the axial magnetic field completely stabilizes all instability modes, the $m=9$ mode becomes the first mode to destabilize ($t=46$ ns); however, the $m=4$ mode has the largest growth rate when the instability bumps are first resolvable ($t=120$ ns). Thus, these higher order modes are expected to develop in the axially magnetized liner-plasma.

IV. CONCLUSION

In this paper, we have presented experimental results for thin-foil, cylindrical plasmas driven with ~600 kA. We showed that: (1) the applied axial magnetic field, irrespective of its direction (e.g., parallel or anti-parallel to the flow of current), reduces the instability amplitude for pure MHD modes (e.g., modes devoid of the acceleration-driven MRT instability); (2) imploding liners (where MHD modes couple to MRT) with applied fields of $B_z=0.5-0.8$ T and $B_z=1.1-2.0$ T generated $m=1$ and $m=2$ helical modes, respectively, which persisted from the implosion to the subsequent explosion stage; (3) the merging of instability structures enabled the re-initiation of an exponential instability growth rate; and (4) an inverse cascade in *both* the axial and azimuthal wavenumbers, k and m, may be responsible for the final $m=2$ helical structure observed in our experiments. These helical modes are phenomenologically consistent with the helical features observed by Awe *et al.*,[11,12] which may be interpreted as $m=5$ and $m=6$ modes that persist as discrete helical modes[8] during the implosion stage. The seeding of these helical modes, whether from noise or from an additional early-time instability, remains an outstanding question, for both university-scale experiments and MagLIF experiments at Sandia National Laboratories.

ACKNOWLEDGMENTS

We thank Dr. Matthew Gomez for helpful technical discussions and the ABZ group at Sandia National Laboratories for donating the Helmholtz-like magnetic field coils utilized in this research. We also thank Geoffrey Greening, Steven Exelby, and Mark Perreault for experimental assistance. This research was supported by the DOE through Award No. DE-SC0012328, Sandia National Laboratories, and the National Science Foundation. D.Y.E. was supported by an NSF fellowship under Grant No. DGE 1256260. The fast framing camera was supported by a DURIP, AFOSR Grant No. FA9550-15-1-0419. Sandia National Laboratories is a multi-mission laboratory managed and operated by National Technology and Engineering Solutions of Sandia, LLC, a wholly owned subsidiary of Honeywell International, Inc., for the U.S. Department of Energy's National Nuclear Security Administration under Contract No. DE-NA-0003525.

[1]D. A. Yager-Elorriaga, P. Zhang, A. M. Steiner, N. M. Jordan, Y. Y. Lau, and R. M. Gilgenbach, Phys. Plasmas **23**, 101205 (2016).
[2]D. A. Yager-Elorriaga, P. Zhang, A. M. Steiner, N. M. Jordan, P. C. Campbell, Y. Y. Lau, and R. M. Gilgenbach, Phys. Plasmas **23**, 124502 (2016).
[3]M. E. Cuneo, M. C. Herrmann, D. B. Sinars, S. A. Slutz, W. A. Stygar, R. A. Vesey, A. B. Sefkow, G. A. Rochau, G. A. Chandler, J. E. Bailey, J. L. Porter, R. D. McBride, D. C. Rovang, M. G. Mazarakis, E. P. Yu, D. C. Lamppa, K. J. Peterson, C. Nakhleh, S. B. Hansen, A. J. Lopez, M. E. Savage, C. A. Jennings, M. R. Martin, R. W. Lemke, B. W. Atherton, I. C. Smith, P. K. Rambo, M. Jones, M. R. Lopez, P. J. Christenson, M. A. Sweeney, B. Jones, L. A. McPherson, E. Harding, M. R. Gomez, P. F. Knapp, T. J. Awe, R. J. Leeper, C. L. Ruiz, G. W. Cooper, K. D. Hahn, J. McKenney, A. C. Owen, G. R. McKee, G. T. Leifeste, D. J. Ampleford, E. M. Waisman, A. Harvey-Thompson, R. J. Kaye, M. H. Hess, S. E. Rosenthal, and M. K. Matzen, IEEE Trans. Plasma Sci. **40**, 3222 (2012).
[4]S. A. Slutz, M. C. Herrmann, R. A. Vesey, A. B. Sefkow, D. B. Sinars, D. C. Rovang, K. J. Peterson, and M. E. Cuneo, Phys. Plasmas **17**, 056303 (2010).
[5]S. A. Slutz and R. A. Vesey, Phys. Rev. Lett. **108**, 025003 (2012).
[6]M. R. Gomez, S. A. Slutz, A. B. Sefkow, D. B. Sinars, K. D. Hahn, S. B. Hansen, E. C. Harding, P. F. Knapp, P. F. Schmit, C. A. Jennings, T. J. Awe, M. Geissel, D. C. Rovang, G. A. Chandler, G. W. Cooper, M. E. Cuneo, A. J. Harvey-Thompson, M. C. Herrmann, M. H. Hess, O. Johns, D. C. Lamppa, M. R. Martin, R. D. McBride, K. J. Peterson, J. L. Porter, G. K. Robertson, G. A. Rochau, C. L. Ruiz, M. E. Savage, I. C. Smith, W. A. Stygar, and R. A. Vesey, Phys. Rev. Lett. **113**, 155003 (2014).
[7]M. R. Gomez, S. A. Slutz, A. B. Sefkow, K. D. Hahn, S. B. Hansen, P. F. Knapp, and C. A. Jennings, Phys. Plasmas **22**, 056306 (2015).
[8]M. R. Weis, P. Zhang, Y. Y. Lau, P. F. Schmit, K. J. Peterson, M. Hess, and R. M. Gilgenbach, Phys. Plasmas **22**, 032706 (2015).
[9]R. D. McBride, S. A. Slutz, C. A. Jennings, D. B. Sinars, M. E. Cuneo, M. C. Herrmann, R. W. Lemke, M. R. Martin, R. A. Vesey, K. J. Peterson, A. B. Sefkow, C. Nakhleh, B. E. Blue, K. Killebrew, D. Schroen, T. J. Rogers, A. Laspe, M. R. Lopez, I. C. Smith, B. W. Atherton, M. Savage, W. A. Stygar, and J. L. Porter, Phys. Rev. Lett. **109**, 135004 (2012).
[10]R. D. McBride, M. R. Martin, R. W. Lemke, J. B. Greenly, C. A. Jennings, D. C. Rovang, D. B. Sinars, M. E. Cuneo, M. C. Herrmann, S. A. Slutz, C. W. Nakhleh, D. D. Ryutov, J. P. Davis, D. G. Flicker, B. E. Blue, K. Tomlinson, D. Schroen, R. M. Stamm, G. E. Smith, J. K. Moore, T. J. Rogers, G. K. Robertson, R. J. Kamm, I. C. Smith, M. Savage, W. A. Stygar, G. A. Rochau, M. Jones, M. R. Lopez, J. L. Porter, and M. K. Matzen, Phys. Plasmas **20**, 056309 (2013).
[11]T. J. Awe, R. D. McBride, C. A. Jennings, D. C. Lamppa, M. R. Martin, D. C. Rovang, S. A. Slutz, M. E. Cuneo, A. C. Owen, D. B. Sinars, K. Tomlinson, M. R. Gomez, S. B. Hansen, M. C. Herrmann, J. L. McKenney, C. Nakhleh, G. K. Robertson, G. A. Rochau, M. E. Savage, D. G. Schroen, and W. A. Stygar, Phys. Rev. Lett. **111**, 235005 (2013).
[12]T. J. Awe, C. A. Jennings, R. D. McBride, M. E. Cuneo, D. C. Lamppa, M. R. Martin, D. C. Rovang, D. B. Sinars, S. A. Slutz, A. C. Owen, K. Tomlinson, M. R. Gomez, S. B. Hansen, M. C. Herrmann, M. C. Jones, J. L. McKenney, G. K. Robertson, G. A. Rochau, M. E. Savage, D. G. Schroen, and W. A. Stygar, Phys. Plasmas **21**, 056303 (2014).
[13]Y. Y. Lau, J. C. Zier, I. M. Rittersdorf, M. R. Weis, and R. M. Gilgenbach, Phys. Rev. E **83**, 066405 (2011).
[14]M. R. Weis, P. Zhang, Y. Y. Lau, I. M. Rittersdorf, J. C. Zier, R. M. Gilgenbach, M. H. Hess, and K. J. Peterson, Phys. Plasmas **21**, 122708 (2014).

[15]R. M. Gilgenbach, M. R. Gomez, J. C. Zier, W. W. Tang, D. M. French, Y. Y. Lau, M. G. Mazarakis, M. E. Cuneo, M. D. Johnston, B. V. Oliver, T. A. Mehlhorn, A. A. Kim, and V. A. Sinebryukhov, AIP Conf. Proc. **1088**, 259 (2009).
[16]D. A. Yager-Elorriaga, A. M. Steiner, S. G. Patel, N. M. Jordan, Y. Y. Lau, and R. M. Gilgenbach, Rev. Sci. Instrum. **86**, 113506 (2015).
[17]A. A. Kim, M. G. Mazarakis, V. A. Sinebryukhov, B. M. Kovalchuk, V. A. Visir, S. N. Volkov, F. Bayol, A. N. Bastrikov, V. G. Durakov, S. V. Frolov, V. M. Alexeenko, D. H. McDaniel, W. E. Fowler, K. LeChien, C. Olson, W. A. Stygar, K. W. Struve, J. Porter, and R. M. Gilgenbach, Phys. Rev. ST Accel. Beams **12**, 050402 (2009).
[18]M. G. Mazarakis, W. E. Fowler, K. L. LeChien, F. W. Long, M. K. Matzen, D. H. McDaniel, R. G. McKee, C. L. Olson, J. L. Porter, S. T. Rogowski, K. W. Struve, W. A. Stygar, J. R. Woodworth, A. A. Kim, V. A. Sinebryukhov, R. M. Gilgenbach, M. R. Gomez, D. M. French, Y. Y. Lau, J. C. Zier, D. M. VanDevalde, R. A. Sharpe, and K. Ward, IEEE Trans. Plasma Sci. **38**, 704 (2010).
[19]D. C. Rovang, D. C. Lamppa, M. E. Cuneo, A. C. Owen, J. McKenney, D. W. Johnson, S. Radovich, R. J. Kaye, R. D. McBride, C. S. Alexander, T. J. Awe, S. A. Slutz, A. B. Sefkow, T. A. Haill, P. A. Jones, J. W. Argo, D. G. Dalton, G. K. Robertson, E. M. Waisman, D. B. Sinars, J. Meissner, M. Milhous, D. N. Nguyen, and C. H. Mielke, Rev. Sci. Instrum. **85**, 124701 (2014).
[20]D. A. Yager-Elorriaga, Ph.D. thesis, University of Michigan, Ann Arbor, 2017.
[21]P. M. Bellan, *Fundamentals of Plasma Physics* (Cambridge University Press, Cambridge, UK, 2006).
[22]L. Atoyan, D. A. Hammer, B. R. Kusse, T. Byvank, A. D. Cahill, J. B. Greenly, S. A. Pikuz, and T. A. Shelkovenko, Phys. Plasmas **23**, 022708 (2016).
[23]S. Atzeni and J. Meyer-Ter-Vehn, *The Physics of Inertial Fusion* (Oxford University Press, NY, 2004).
[24]M. R. Douglas, C. Deeney, and N. F. Roderick, Phys. Plasmas **5**, 4183 (1998).